Available online at www.sciencedirect.com

jmr&t Journal of Materials Research and Technology

journal homepage: www.elsevier.com/locate/jmrt

Original Article

Efficient fabrication and characterization of Ni-Fe-WC composite coatings with high corrosion resistance

Hui Jin, Renjie Ji, Tiancong Dong, Shuo Liu, Fan Zhang, Lilong Zhao, Chi Ma, Baoping Cai, Yonghong Liu*

College of Mechanical and Electronic Engineering, China University of Petroleum (East China), Qingdao, Shandong, 266580, PR China

ARTICLE INFO

Article history:
Received 17 September 2021
Accepted 27 November 2021
Available online 2 December 2021

Keywords:
Nickel-iron alloy
Jet electrodeposition
Composite coating
Corrosion resistance
WC particles

ABSTRACT

Nickel-iron alloy is broadly utilized in the industrial field due to its fabulous mechanical properties. How to prepare nickel-iron alloy with better corrosion resistance more efficiently is an important concern. Based on this, the WC particles enhanced nickel-iron coatings were fabricated by jet electrodeposition (JED) at a high current density of 100A/dm^2. It was found that increasing the deposition temperature appropriately during JED is beneficial to obtain Ni-Fe-WC coating with the higher number of hard particles. Specifically, the maximum WC particles proportion reaches 4.47 wt% at 55 °C. The electrochemical corrosion behavior of coating was measured by polarization curve and electrochemical impedance spectroscopy (EIS). The polarization curve test results displayed that the E_{corr} positively shifted from −0.402 to −0.281 V and the i_{corr} reduced from 25.13 to 7.05 μA/cm^2 with the increase of WC particles proportion. Meanwhile, the EIS test results exhibited that the impedance of coating enhanced from 12,720 to 59,140 Ω cm^2. The neutral salt spray test (NSS) was used to simulate the corrosion of coating in a seawater environment. The NSS results showed that with the increase of WC particles, the corrosion products decreased gradually and the degree of corrosion decreased. The analysis showed that WC particles can help the grain growth and release the internal stress in the coating. Larger grain sizes reduces intergranular corrosion and smaller internal stress help to alleviate stress corrosion cracking. The above research can provide theoretical support for the efficient preparation of particle enhanced composite coating with strong corrosion resistance.

Abbreviations: JED, Jet electrodeposition; CED, Conventional electrodeposition; NSS, Neutral salt spray test.

* Corresponding author.
E-mail address: jirenjie@163.com (R. Ji).

https://doi.org/10.1016/j.jmrt.2021.11.145

1. Introduction

Corrosion is the main cause of material failure of key mechanical components, which more often than not leads to financial misfortunes, security mishaps, and indeed casualties [1]. In arrange to extend the service life of machine parts in unforgiving situations, different surface modification technologies and unused surface security materials have gradually been developed. Ni–Fe alloy has been broadly utilized in the field of industrial anti-corrosion because of its fabulous corrosion resistance, mechanical properties, and relatively low price [2–5]. The preparation methods of Ni–Fe alloys include spraying [6], laser remelting [7], sintering [8], vacuum melting [9], electrodeposition methods [10–14], etc. Among them, electrodeposition is the foremost common strategy because it can deposit nanostructure coatings with better performance on many conductive substrates and is simple to operate. During the preparation of alloy coatings, the deposition temperature is an important factor that affects the structure and performance of the coatings. Cui et al. [15] found that as the temperature of the electrolyte increases, the thermodynamic stability of the obtained coating is significantly improved and the structure is denser when the Ni–P alloy is electrodeposited. Rai et al. [16] found that when the deposition temperature is low, the diffusion and solubility of graphite are lower, and the prepared Ni-graphite coating is thinner. As the temperature rises, the diffusion and solubility of graphite become higher, and the obtained composite coating is thicker and denser. Lee et al. [17] found that the electrolyte temperature has a significant effect on the phase structure and stability of the coating during the preparation of Fe–Ni alloy. Specifically, as the temperature increases, the effect of abnormal co-deposition gradually weakens, the content of Fe gradually decreases, and the high temperature stability of the obtained coating is better. Oliveira et al. [18] found that the deposition temperature has a greater influence on the alloy composition when electrodepositing Ni–W–Co coating. As the temperature increases, the ion mobility increases, which is beneficial to the reduction of Ni and Co in the coating and the improvement of the coating. Seo et al. [19] studied the effect of temperature on the Ni–Fe–P alloy electrodeposited by sulfanilic acid. When the temperature is increased to 60 °C, the sulfur content in the coating decreases. When the electrolyte temperature is increased from 60 °C to 70 °C, the residual stress of the coating is significantly reduced, and the resistance of the coating is greatly improved. From the above research, it can be known that in the process of electrodeposition of Ni-based alloy or Ni–Fe-based alloys, the content of various elements in the coating can be controlled by adjusting the temperature. However, there are few studies on the mechanism of temperature on the deposition of particles in composite coatings, and the mechanism analysis of deposition temperature on the composition and performance of the coating needs further research.

In recent years, the research on the preparation of particle reinforced composite coatings by electrodeposition has attracted the attention of researchers because the doped hard particles can effectively improve the comprehensive properties of Ni–Fe alloy coatings. Starosta et al. [20] found that the addition of Al_2O_3 nanoparticles is beneficial to strengthen the structure of Ni–Fe coating and significantly improve the mechanical performances of the coating. Li et al. [21] demonstrated that the content of ZrO_2 affects the composition and structure of the coating. Particularly, with the increment of ZrO_2 particles, the roughness and corrosion resistance of Ni–Fe coating also expanded. Safavi et al. [13] found that the addition of Y_2O_3 nanoparticles makes coating more compact, which results in the prepared Ni–Fe–Y_2O_3 composite coating having excellent performance of anticorrosion. Yousefi et al. [10] prepared Ni–Fe–TiO_2 composite coatings and examined the impact of current on the coating performance. The results showed that with the increment of current, the number of TiO_2 nanoparticles increased, and the corrosion resistance of the coating was positively correlated with the content of TiO_2

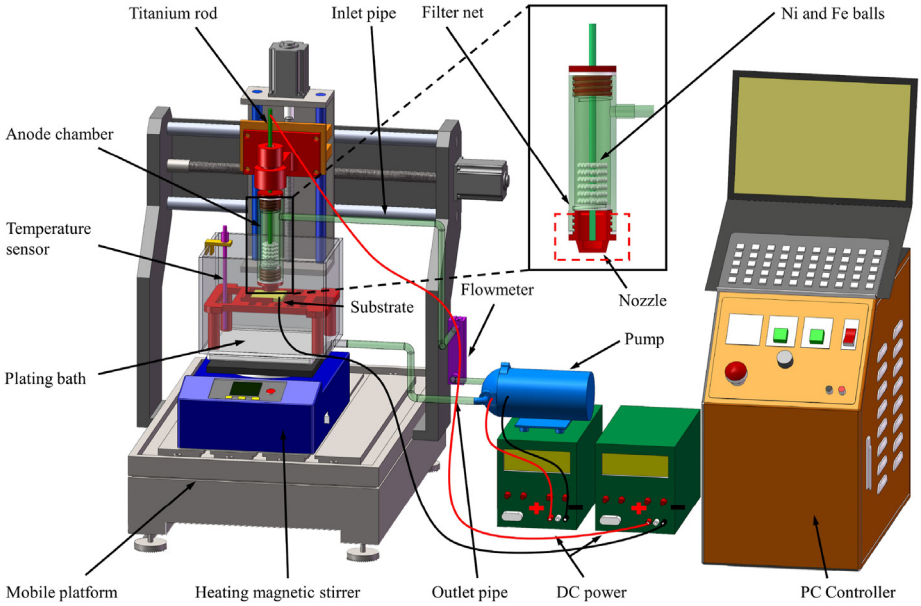

Fig. 1 – Schematic diagram of experimental equipment.

particles. Rasooli et al. [22] evaluated the relationship between the Ni–Fe–Cr_2O_3 coating properties and the concentration of the particles within the plating solution. The results showed that the coating with 6 g/L Cr_2O_3 particles concentration has the best performance.

The above research focuses on the introduction of hard particles in the conventional electrodeposition (CED) process to strengthen the performance of Ni–Fe coating, and just explores the relationship between the concentration of hard particles and the performance of the coating. Because the diameters of those hard particles are all micro and nano grades, they have higher surface energy, which makes most of them exist within the plating solution in the agglomerated form [23,24]. During the CED, it is difficult to break this agglomerated state, and finally obtain a composite coating with uneven particle distribution, which isn't conducive to the enhancement of coating properties. JED is a high-speed electroplating technique carried out in a part of the substrate [25,26]. As an unconventional electrodeposition technology, compared with CED, the high-speed flushing process can destroy the agglomerated hard particles effectively when preparing particle-reinforced composite coatings. Therefore, the prepared coating by JED has excellent characteristics of high preparation efficiency, uniform distribution of nanoparticles, and tall surface quality [27,28]. In recent years, researchers have also researched on the preparation of particle-enhanced coatings by JED. Xia et al. [29] prepared Ni–TiN films by JED and explored the corrosion properties of the film. The results indicated that Ni–TiN film prepared at the 5 g/L TiN addition has minimum corrosion potential and corrosion current. Ji et al. [27] prepared the Ni-graphene films and explored the key parameters of the JED. Results indicated that the mechanical and corrosion resistance of coating achieved best when the concentration of graphene was 0.5 g/L. Wang et al. [30] fabricated Ni–CeO_2 coatings and explored the relationship between CeO_2 nanoparticles and the properties of the coating. The comes about appeared that the coating with higher CeO_2 nanoparticles had fewer surface defects and better corrosion resistance. Jiang et al. [31] fabricated Ni–SiC coatings through magnetic field-assisted JED and found that the addition of a magnetic field would increase the number of SiC particles of the coating. Meanwhile, the wear resistance of coating was also improved accordingly. Ma et al. [32] fabricated Ni–AlN coatings by JED with ultrasound technique and found that the addition of ultrasound made the coating structure more compact. The results showed that the friction performance of coating was enhanced with the content of AlN particles increased.

The above researches about the fabrication of particle-reinforced coatings by JED mainly focus on single metal composite coatings, and there are little researches on alloy composite coatings. Moreover, these investigations tend to explore the effect of particles content on the coating performance or add some auxiliary means to improve the content of hard particles. The mechanism of deposition of hard particles during JED has not been studied in depth. Based on the above analysis, this study prepared the Ni-Fe-WC composite coatings by JED and found that coatings with more WC particles have better corrosion resistance. At the same time, the mechanism of WC particles adsorption during the fabrication of particle-reinforced composite coatings during JED and the impact of WC particles on the corrosion resistance were deeply analyzed. Some innovative theories and technical results were obtained.

2. Materials and methods

2.1. *Experimental equipment*

Figure 1 shows the experimental equipment diagram. The cathode of DC supply links to the substrate and the anode connects to the titanium rod. Due to the stable chemical properties of titanium, the titanium rod is not consumed

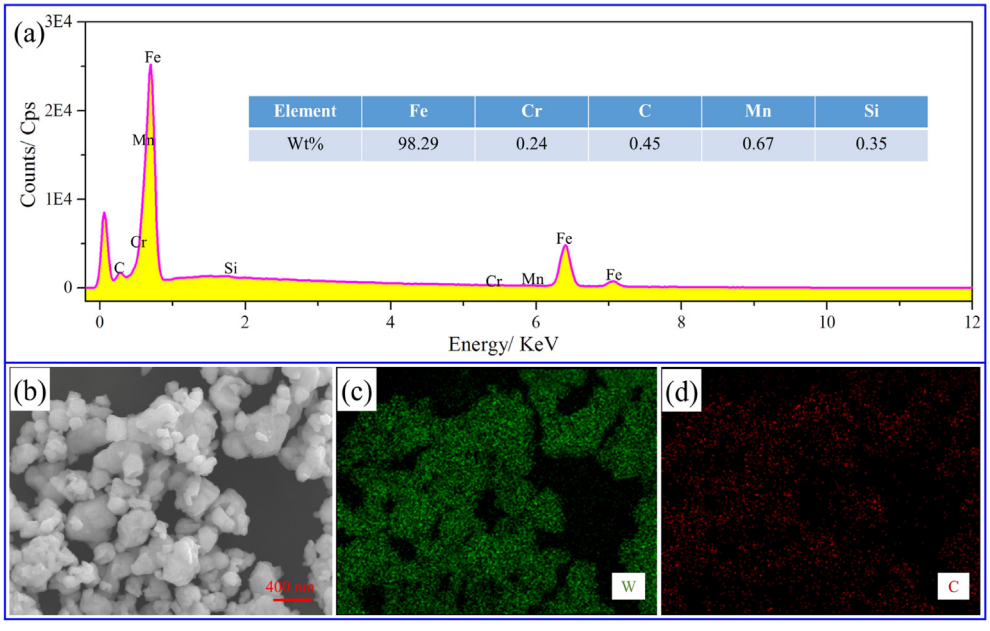

Fig. 2 – (a) The composition of substrate, (b) SEM image of WC particles, (c–d) EDS mapping images of WC particles.

during the electrodeposition process. At the same time, the distance between the titanium rod and the substrate is relatively close. The stable current distribution makes the electrodeposition process more stable. The plating solution is sprayed from the nozzle into the surface of the substrate at a high speed, and the unreacted plating solution is magnetically stirred and heated in the plating bath to prevent the WC nanoparticles from agglomerating. The function of the diaphragm pump is to circulate the plating solution and control the flow rate of the bath.

2.2. Experimental parameters

The substrate material is medium carbon steel, and its composition is shown in Fig. 2(a). Before the experiment, the substrate is pretreated as follows: first, use a grinder to remove the oxide layer and rust on the surface, then use 400, 800, 1200, 1500, 2000 mesh sandpaper and nylon polishing cloth for polishing, and finally ultrasonically clean with alcohol for 30 min and dry. Figure 2(b) is the SEM image of WC particles with a mean diameter size of 300 nm. Figure 2(c and d) is the EDS mapping images of WC particles. The composition of the plating solution is as follows: 300 g/L of $NiSO_4 \cdot 6H_2O$, 40 g/L of $NiCl_2 \cdot 6H_2O$, 20 g/L of $FeCl_2 \cdot 4H_2O$, 20 g/L of H_3BO_3, 0.5 g/L of saccharin, 1.0 g/L of emulsifier OP-10, and 25 g/L of WC particles. All reagents were purchased from Aladdin Biochemical Technology Co., Ltd., with a purity of 99.9%. The solvent is deionized water. Table 1 shows the experimental parameters of JED.

2.3. Characterization methods

The surface morphology Ni-Fe-WC coating was demonstrated utilizing SEM. The elements distribution and compound structure of coating were characterized utilizing EDS and XPS. The crystal structure and grain size of coating were measured utilizing XRD. The surface 3D profile of coating were observed utilizing a hyper-depth 3D microscope. The electrochemical corrosion characteristics of Ni-Fe-WC coatings were evaluated by polarization curve and EIS. The test solution was 3.5wt% NaCl solution and the test environment was room temperature. All the tests were carried out in a three-electrode system, with a reference electrode of Ag/AgCl, a counter electrode of platinum plate, and a working electrode of coating. The polarization curve was recorded in the range of −300 to +300 mV (relative to E_{ocp}) with a 1 mV/s scan rate. The EIS was recorded in the range of 10^5 to 10^{-2} Hz with 10 mV sinusoidal signal amplitude. The environmental corrosion behavior of coating in the salt environment was measured by NSS experiment. The concentration of the NaCl salt solution was 5wt%, the pH value was 7, the temperature was 35 °C, the sedimentation volume after atomization was 2 mL/(h·cm^2).

Table 1 – The experimental parameters of JED.

Experimental parameters	Quantity
pH value of plating solution	4
Size of jet nozzle/mm	1 × 15
Speed of jet nozzle/mm·min^{-1}	100
Gap between jet nozzle and cathode/mm	5
Flow rate of plating solution/L·min^{-1}	1.5
Current density/A·dm^{-2}	100
Temperature/°C	25, 35, 45, 55, 65

3. Results

3.1. Composition of coating

The EDS images of coatings are shown in Fig. 3. As shown in Fig. 3 (a-e), it is clear that all coatings just contain Ni, Fe, W, C, and O elements. The mass percentage of WC particles can be obtained by converting the W element content. According to Fig. 3(f), as the deposition temperature rises from 25 °C to 65 °C, the content of WC particles is 0.53, 0.64, 0.73, 4.47, and 4.16 wt%, respectively.

The deposition rate of Ni^{2+}, Fe^{2+}, and WC particles at different temperatures are calculated using the weighing method. The samples were deposited for 30 min at different deposition temperatures. The weight difference of the samples before and after deposition is the coating weight, and the coating weight divided by the time is the coating deposition rate. The deposition rate of Ni^{2+}, Fe^{2+}, and WC particles can be obtained by multiplying the deposition rate of the coating with the percentage of Ni, Fe, and WC particles in the coating, respectively. The above experiment is performed 5 times and the average value is taken. The measurement results are shown in Fig. 4(a). It is found that the deposition rate of metal ions and WC particles increase with the increase of temperature. The main reason for this phenomenon is that increasing the temperature can weaken the hydration of ions and reduce the viscosity of the solution, which can increase the particle movement speed, thereby increasing the conductivity of the solution, and finally improve the reduction speed of ions [15,18]. It can be seen from Fig. 4(b) that when the deposition temperature is lower than 55 °C, the percentage of deposition rate increment of Ni^{2+} and Fe^{2+} is lower than that of WC, which leads to WC particles content in the coating increases as temperature increases. However, when the deposition temperature is greater than 55 °C, the percentage of deposition rate increment of Ni^{2+} and Fe^{2+} is higher than that of WC particles, so the WC particles content in the coating decreases slightly as temperature increases.

The XRD spectra of the Ni-Fe-WC coatings are shown in Fig. 5. The Fitting illustrate that all coatings are (Ni, Fe) face-centered cubic structure with significant (111), (200), (220) intensity peaks. When the temperature is 55 °C and 65 °C, the peak of the WC phase appear in the XRD pattern of the prepared coating, while do not appear at other temperatures, because the particles content in the coating is detected when it is higher than a certain value [30,33].

The XPS test results of the Ni-Fe-WC coatings are shown in Fig. 6. From the XPS survey spectra (Fig. 6(a)), it is clear that all coatings have obvious C_{1s}, O_{1s}, W_{4s}, Fe_{2p}, Ni_{2p} peaks, which are mutually verified with the results in Fig. 3. From the high-resolution XPS spectra of Ni_{2p} (Fig. 6(b)), It can be seen that there is an obvious intensity peak of about 852.9 eV, which corresponds to the $2p_{3/2}$ peak of Ni [34]. According to the standard binding energy (Ni metal: 852.6 eV, NiO: 853.7 eV). It can be considered that the Ni element composition on the

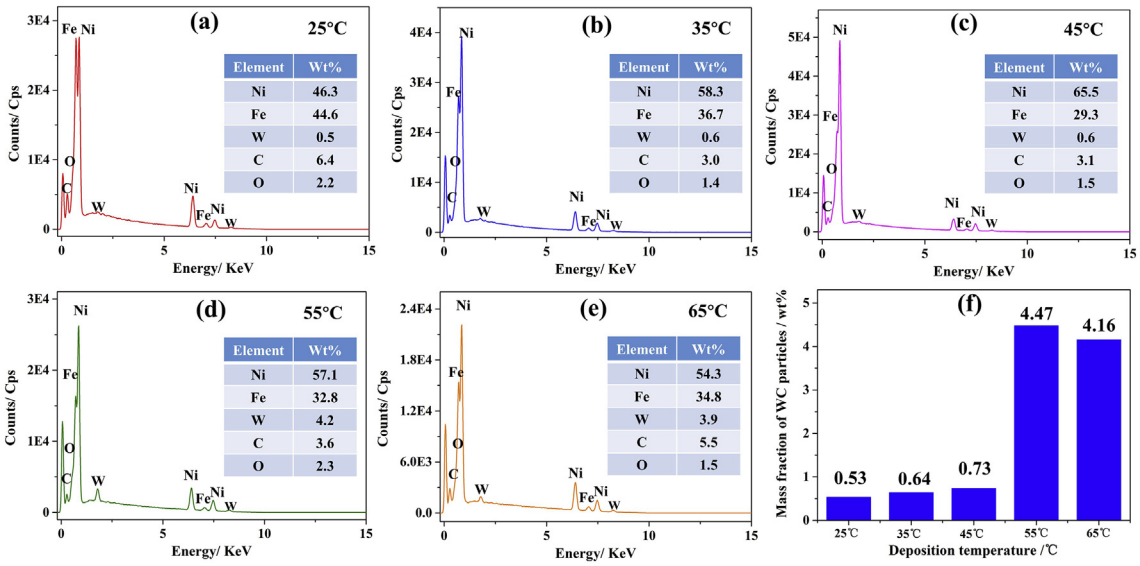

Fig. 3 – The EDS images of Ni-Fe-WC coatings.

surface of the coating is Ni metal and a few parts of NiO. From the high-resolution XPS spectra of Fe_{2p} (Fig. 6(c)), it can be seen that there are two obvious intensity peaks 707.0 and 709.8 eV, which corresponds to the $2p_{3/2}$ peaks of Fe [35]. According to the standard binding energy (Fe metal: 706.7 eV, FeO: 709.6 eV, Fe2O3: 710.8 eV). It can be considered that the Fe element composition on the surface of the coating is mainly a large mainly Fe metal, and a small part of iron oxide. In summary, the prepared Ni-Fe-WC coating mainly consists of Ni, Fe, WC particles, and a small amount of metal oxides.

3.2. *Surface morphology of coating*

The SEM images and 3D morphologies of coatings are shown in Fig. 7. The surface morphologies and roughnesses of those coatings are significantly different. When the temperature is 25 °C, a large number of bulges larger than 6 μm appear on the surface. The microstructure of the coating shows a grind arenaceous texture, and the maximum profile difference of the surface is 8.09 μm (Fig. 7(a-b)). When the temperature is 35 °C, the size of the bulges is reduced to 3–5 μm, and the number of bulges is reduced. The microstructure of the coating still shows a grind arenaceous texture, and the maximum profile difference of the surface is 6.91 μm (Fig. 7(c-d)). When the temperature is 45 °C, the size of the bulges is reduced to 2–4 μm. The microstructure of the coating shows a smooth texture, and the maximum profile difference of the surface is 5.92 μm (Fig. 7(e-f)). When the temperature is 55 °C, the size of the bulges is 2–4 μm, but the number of bulges increases sharply, even stacking together to form agglomerates, and the profile height difference of the surface is 15.70 μm (Fig. 7(g-h)). When the temperature is 65 °C, the morphology of the coating surface is consistent with the deposition temperature of 55 °C, and the maximum height difference of the coating surface profile is 12.66 μm (Fig. 7(i-j)).

Combined with Fig. 3(f) and Fig. 7, it can be concluded that when the temperature is relatively low, the surface roughness of the coating decreases with the temperature increases, indicating that increasing the temperature appropriately can effectively improve the surface quality of the coating.

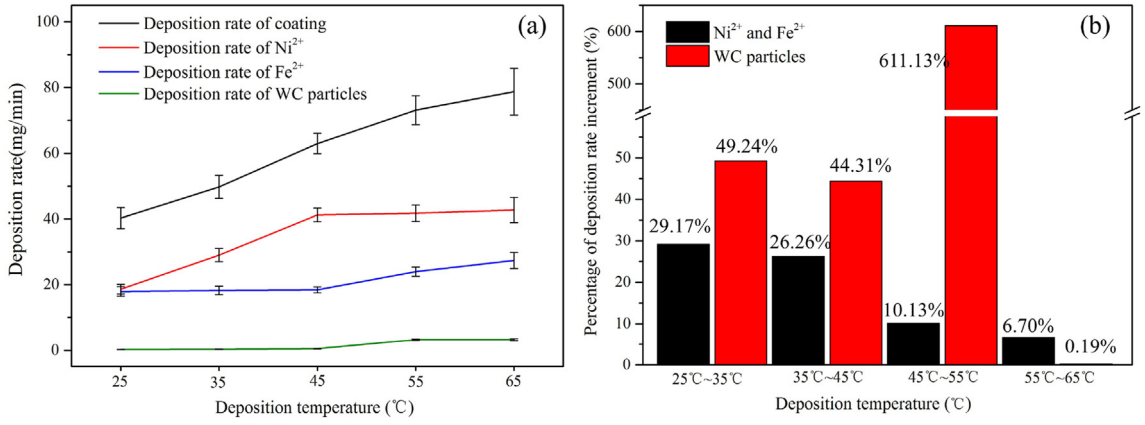

Fig. 4 – (a) The deposition rates of Ni2+, Fe2+ and WC particles at different temperatures, (b) the percentage of deposition rate increment of metal ions and WC particles.

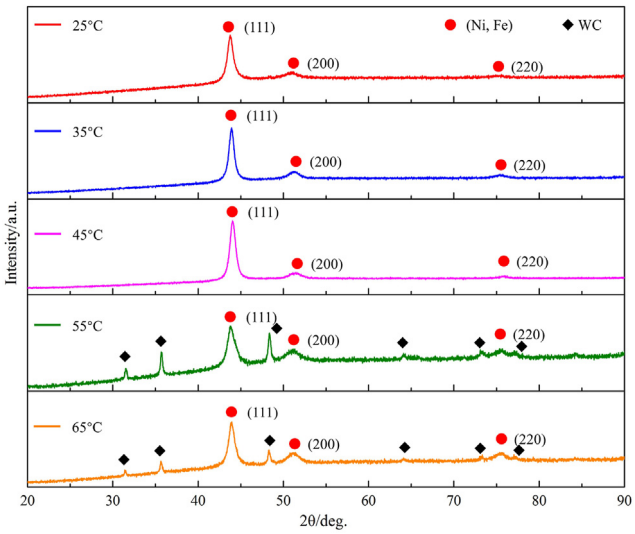

Fig. 5 – The XRD spectra of Ni-Fe-WC coatings.

However, when the temperature achieves above 55 °C, the coating suddenly develops a large number of bulges. From the scanning diagram of the W element distribution of the high magnification coating, it can be seen that the content of large WC particles in the bulge is significantly higher than that in the flat. When bulges gather, WC particles are also prone to agglomeration, which leads to the increase of coating roughness.

3.3. *Electrochemical behavior of coating*

The electrochemical corrosion behavior of coating was obtained by measuring the polarization curve and EIS. The corrosion potential (E_{corr}) and corrosion current density (i_{corr}) of the coating were obtained by fitting the polarization curve. The high E_{corr} and low I_{corr} reveal that the coating has excellent corrosion resistance. It is obvious from Fig. 8 that as the temperature increments from 25 °C to 65 °C, the E_{corr} is −0.402, −0.335, −0.303, −0.281, −0.295 V, and the I_{corr} is 25.13, 16.61, 13.92, 7.05, 8.23 μA/cm^2, respectively. The corrosion resistance of coating increases first and then decreases with the increase of temperature, which is consistent with the law that the WC particles content changes with temperature. The coating prepared at 55 °C has the best corrosion resistance.

The electrochemical reaction of the coating/electrolyte interface during electrochemical corrosion can be obtained by the EIS method. The EIS spectrum includes Bode diagram or Nyquist diagram forms [36–38]. Nyquist diagrams are composed of incomplete semicircular arcs. Generally speaking, the larger the diameter of the arc, the better the anti-corrosion performance of the coating. As shown in Fig. 9(a), the diameter of the arc increases first and then decreases with the increase of temperature. The Bode diagrams of log(f) vs. log(|Z|) are shown in Fig. 9(b). In 10^3–10^5 Hz frequency range, the values of log|Z| are about 20 Ω cm^2, which represents the solution impedance. In the 10^{-2}–10^3 Hz frequency range, the values of log|Z| increase as the frequency decreases, which represents the impedances of Ni-Fe-WC coatings. At the fixed 0.01 Hz, as the temperature increases, the value of polarization impedance is 12,720, 14,320, 15,470, 57,850, and 59,140 Ω cm^2, respectively.

The Bode diagrams of log(f) vs. angle are shown in Fig. 9(c), with the temperature increases, the maximum phase angle is 68.9, 71.2, 74.8, 80.9, and 80.4°, respectively. The higher polarization impedance and the bigger phase angle indicate the capacitance property of coating better. The better the capacitance of the coating is, the better the corrosion resistance is.

An equivalent circuit (EEC) can replace the reaction at the electrode/solution interface during EIS testing. The EEC obtained by using ZSimpWin software to fit the EIS test results is shown in Fig. 9(d). In the EEC, R_s, R_c, and R_{ct} are the solution resistance, the coating resistance, and the charge transfer resistance, respectively. CPE_1 and CPE_2 are constant phase elements and their impedance can be obtained by $Q = [Y(j\omega)^n]^{-1}$, where Y stands the CPE admittance, j stands the imaginary number ($\sqrt{-1}$), w stands angular frequency (rad s^{-1}), and n stands a value of 0–1. The CPE stands for pure capacitance when n = 1. The fitting parameters of EEC are

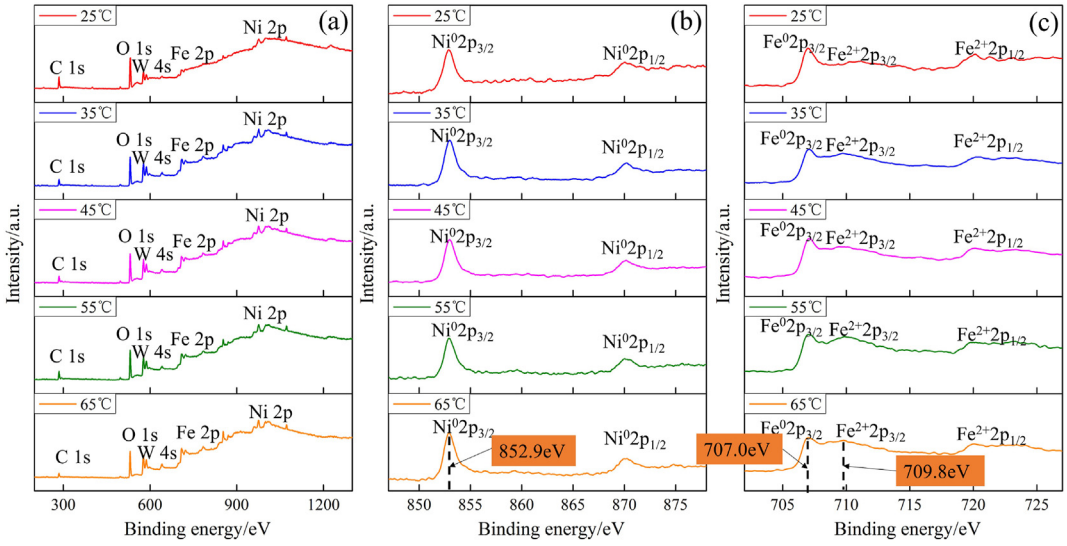

Fig. 6 – The XPS test results of the Ni-Fe-WC coatings: (a) survey spectra, (b) Ni 2p, (c) Fe 2p.

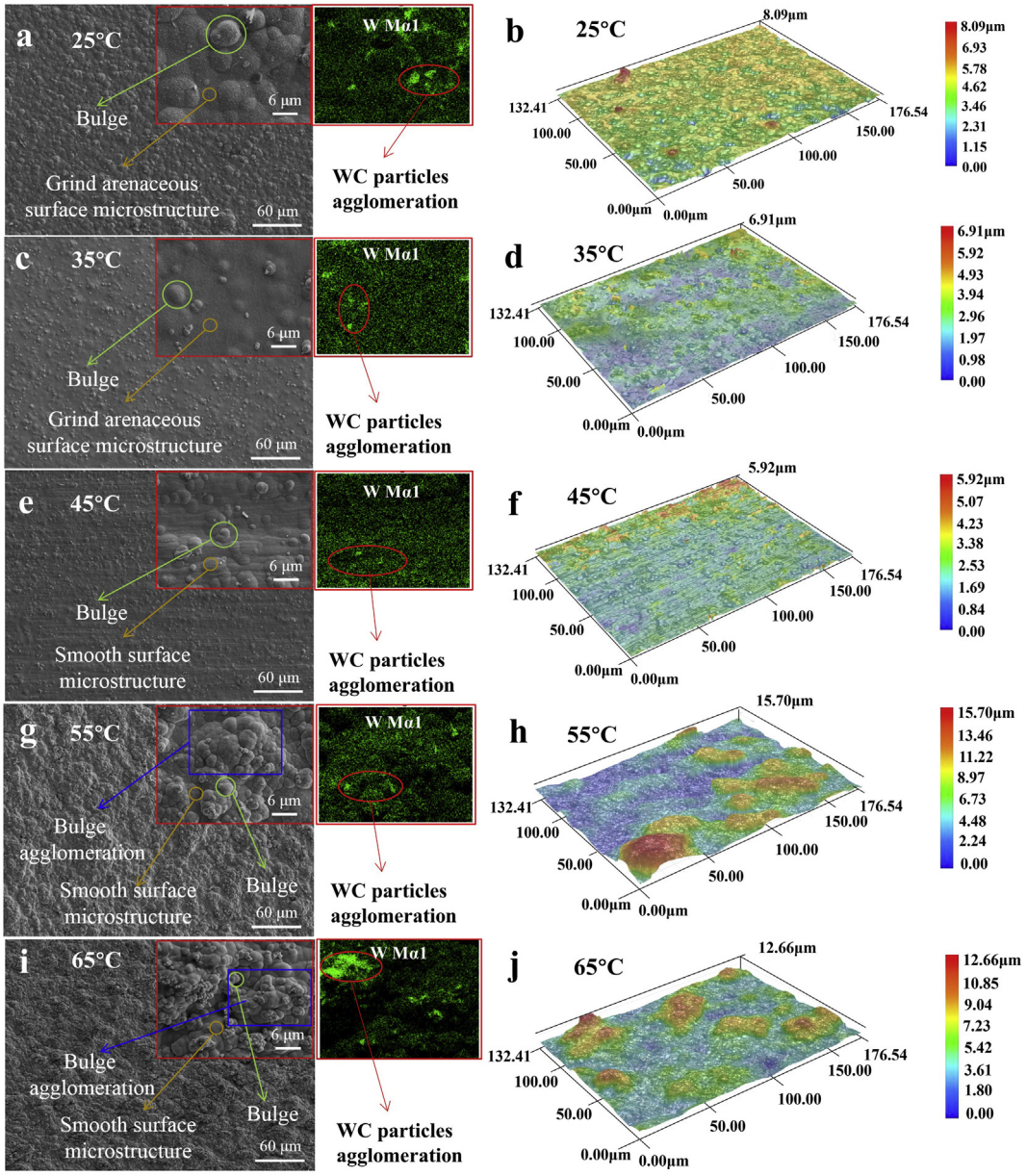

Fig. 7 – SEM images and 3D morphologies of Ni-Fe-WC coatings.

shown in Table 2. All fitting errors are less than 5%, which proves that the EEC is suitable for all coatings. As the temperature rises from 25 to 65 °C, the n value of CPE_1 is 0.8863, 0.8819, 0.9256, 0.8402, and 0.8710, respectively, while the n values of CPE_2 are all 1. The coating surface roughness affects the n value of CPE_1. The larger the roughness is, the smaller the n value is, which is consistent with the change rule in Fig. 7. As the temperature rises from 25 to 65 °C, the R_c is 8.555×10^3, 1.233×10^4, 1.246×10^4, 5.095×10^4 and $4.842 \times 10^4\ \Omega\ cm^2$, and the R_{ct} is 4.058×10^3, 5.377×10^3, 5.829×10^3, 1.538×10^4 and $1.465 \times 10^4\ \Omega\ cm^2$, respectively. It is obvious that the R_p ($R_c + R_{ct}$) of the coating increases first and then decreases with the temperature increases, which is the same as the law that the WC particles content changes with temperature.

3.4. *NSS corrosion behavior of coating*

The NSS duration of coating is 10, 20, and 40 days, respectively. Figure 10 shows the quality changes of coatings after corrosion. It can be found that the corrosion products gradually increase with the increment of the corrosion time. In the same corrosion time, the corrosion products show a trend of first decreasing and then increasing as the deposition temperature increases. When the temperature is 55 °C, the prepared Ni-Fe-WC coating has the least corrosion products.

Figure 11 shows the optical images of the corroded coatings. It is clear that as the corrosion time increases, the corrosion degree of the coating surface intensifies. When the corrosion time is 40 days, each coating shows a significantly different degree of corrosion, according to the degree of

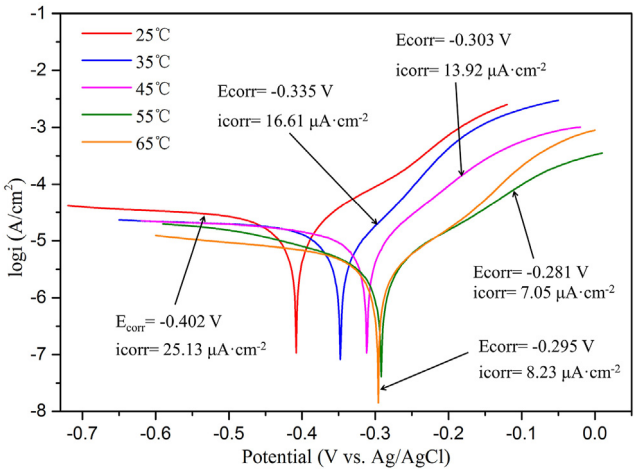

Fig. 8 – The polarization curves of coatings.

corrosion from mild to severe corrosion is divided into the areas of mild corrosion (**A1**), moderate corrosion (**A2**), and severe corrosion (**A3**). As shown in Fig. 12, after 40 days of NSS, the corrosion morphologies of the coatings have obvious differences.

In the mild corrosion areas (**A1**), all the coatings show the flocculent corroded surface, and the coatings are not completely covered due to fewer corrosion products. Through the analysis of EDS (Fig. 13), the O content of **A1** all has increased compared with that before corrosion, indicating that the corrosion products are metal oxides. Meantime, the O content decreased first and then increased with the temperature rising. The less the O content, the fewer the corrosion products and the least corrosion.

In the moderate corrosion areas (**A2**), all surfaces of the coatings are uniformly corroded. When the deposition temperature is low (25°C–45 °C), numerous corrosion holes show up on the surface. When the temperature is higher (55°C–65 °C), there are without corrosion holes that appear on the surface. The more corrosion holes, the easier the corrosion will extend to the depth of the coatings. By observing the EDS spectrum images of **A2** areas (Fig. 13), it is found that the O content in these areas has been increased again, indicating that the degree of oxidation is further intensified (Compared to **A1**). As the deposition temperature increases, the O content shows a trend of first decreasing and then increasing.

In the severe corrosion areas (**A3**), the corrosion products are significantly increased. By observing the EDS spectrum images of the coatings, it is found that the O element contents of all coatings reach the highest (compared to **A1** and **A2**). A large number of corrosion products even form an oxide film, which can effectively prevent the air from contacting the coating for further oxidation. However, with the continuous corrosion process, the internal stress of the coating is released and it is easy to cause cracking of the oxide film. When the deposition temperature is low (25°C–45 °C), the oxide film is loose and there are more cracks. When the deposition temperature is higher (55°C–65 °C), the oxide film is dense and there are fewer cracks. The greater the internal stress of the coating, the more cracks will be caused. Cracks more easily lead to corrosion to the depths of the coating, accelerating the failure of the coating. When the deposition temperature is 55 °C, the oxide film is the densest and the number of cracks is

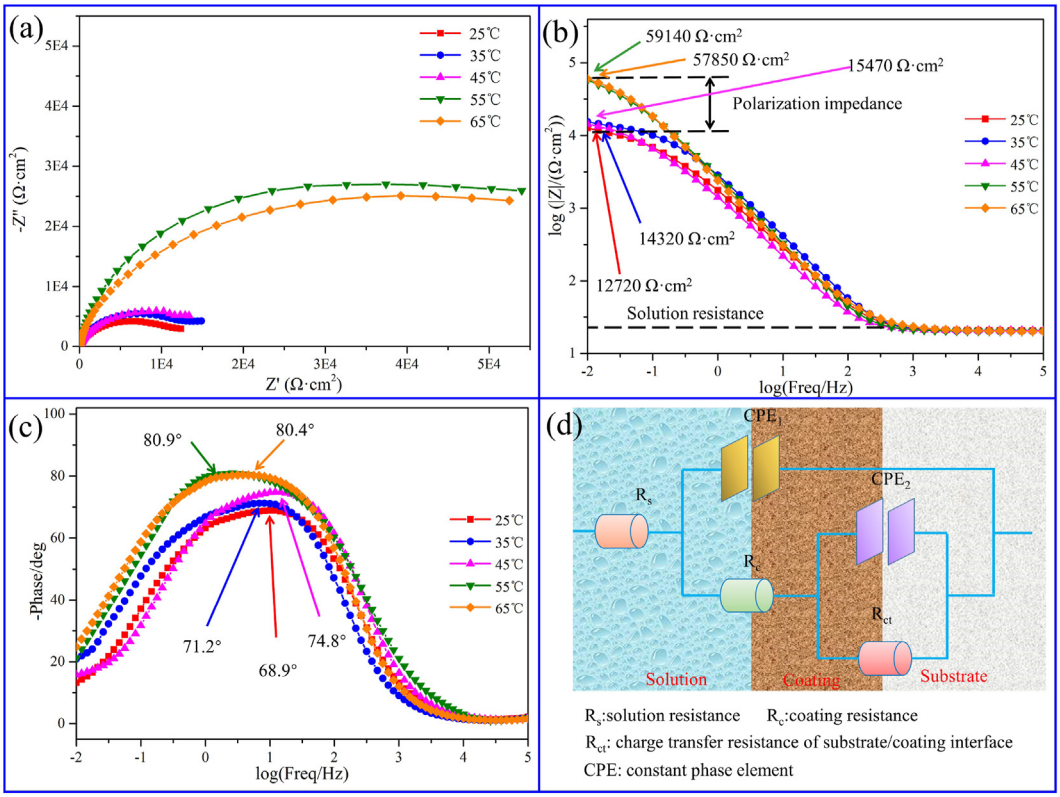

Fig. 9 – (a) Nyquist diagrams, (b–c) Bode diagrams and (d) EEC diagram of Ni-Fe-WC coatings.

Table 2 – Fitting parameters of EEC.

Temperature/°C	$R_s/\Omega\cdot cm^2$	CPE_1		$R_c/\Omega\cdot cm^2$	CPE_2		$R_{ct}/\Omega\cdot cm^2$	Error/%
		$Y_1(S\cdot cm^{-2}\cdot s^n)$	n		$Y_1(S\cdot cm^{-2}\cdot s^n)$	n		
25	20.31	1.110×10^{-5}	0.8863	8.555×10^3	3.644×10^{-5}	1	4.058×10^3	4.139
35	19.93	1.341×10^{-5}	0.8819	1.233×10^4	3.603×10^{-5}	1	5.377×10^3	3.294
45	19.98	6.458×10^{-5}	0.9256	1.246×10^4	4.194×10^{-5}	1	5.829×10^3	1.798
55	20.12	7.926×10^{-5}	0.8402	5.095×10^4	8.010×10^{-5}	1	1.538×10^4	3.574
65	20.18	6.689×10^{-5}	0.8710	4.842×10^4	6.986×10^{-5}	1	1.465×10^4	2.856

the least, which can most effectively prevent the corrosion from occurring in the depth of the coating.

It can be concluded from Figs. 10–13 that the corrosion resistance of Ni-Fe-WC coating prepared at different temperatures after NSS is significantly different. Specifically, with the temperature rising, the corrosion resistance first strengthens and then weakens. This is again consistent with the variation of WC particles content within the coating with temperature.

4. Discussion

According to the section of results, it can be concluded that increasing the content of WC particles within the coating is beneficial to enhance the corrosion resistance of Ni-Fe-WC coating. However, there was no specific explanation for the promotion of corrosion resistance. Therefore, the reason why WC particles enhance the corrosion resistance of Ni-Fe-WC coating is systematically discussed in this section.

4.1. *Influence of WC particles on the coating structure*

The grain orientation coefficient is calculated by the formula (1) [36], where $I_{(hkl)}$ presents the (hkl) plane measured intensity of XRD spectrum, $I_{0(hkl)}$ presents the Ni–Fe alloy powder diffraction intensity.

$$TC(hkl) = \frac{I_{(hkl)}/I_{0(hkl)}}{\sum_{i=1}^{n} I_{(hkl)}/I_{0(hkl)}} \quad (1)$$

The average grain size of coating is calculated by the formula (2) and formula (3) [39], where K presents a constant, γ presents the Cu-Kα wavelength, B presents the diffraction peak half height width, and θ presents the Bragg angle.

$$D(hkl) = \frac{K\gamma}{B\cos\theta} \quad (2)$$

$$D_{avg} = \sum D(hkl)\cdot TC(hkl) \quad (3)$$

It can be found from Fig. 14 that when the temperature increases from 25 °C to 65 °C, the WC particles content increases first from 0.53 wt% to 4.47 wt% and then decreases to 4.15 wt%. As the WC particles content increases, the grain orientation of grain exchanges from (111) to (220). The TC(220) of coating reaches a maximum of 42.2% when the temperature is 55 °C. At the same time, the average grain size of coating is 12.20, 13.70, 14.13, 19.22, and 17.76 nm, respectively. The average size of coating grains is proportional to the WC particles content, which indicates that WC particles have the positive effect on promoting the grain growth of Ni-Fe-WC coating.

4.2. *Influence of WC particles on the coating internal stress*

During the electrodeposition process, the rapidly reduced metal atoms will adsorb on the surface of the substrate, and then the metal atoms will rapidly nucleate and grow to form the coating, but the internal stress is prone to occur during this process [40,41]. The coating internal stress is proportional to the deposition speed and increasing the temperature will accelerate the deposition rate, so the internal stress increases with the rise of the temperature.

According to Fig. 15, when the temperature is below 45 °C, with the increase of temperature, the (111), (200), and (220) peaks all shift to a large angle, indicating that the lattice and the interplanar spacing of the coating become smaller. In this case, it shows that there is internal stress within the Ni-Fe-WC coating, and the internal stress intensifies with the increment of offset angle. However, when the deposition temperature reaches 55 °C and 65 °C, the (111), (200), and (220) peaks of the coating shift to a small angle, indicating that the lattice and the interplanar spacing becomes larger, the internal stress in the coating decreases. When residual stress exists in the coating, the distance between crystal planes will change and the diffraction peak will also change accordingly. The movement of the diffraction peak is related to the residual stress. The sin2ψ method proposed by E. Mchearauch is used to

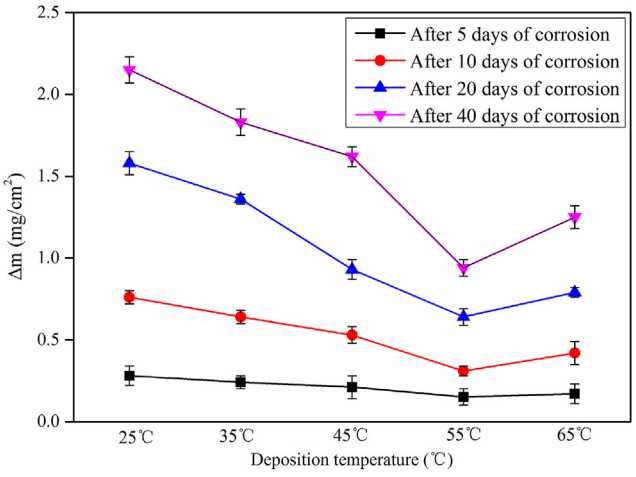

Fig. 10 – The quality changes of the Ni-Fe-WC coatings after NSS.

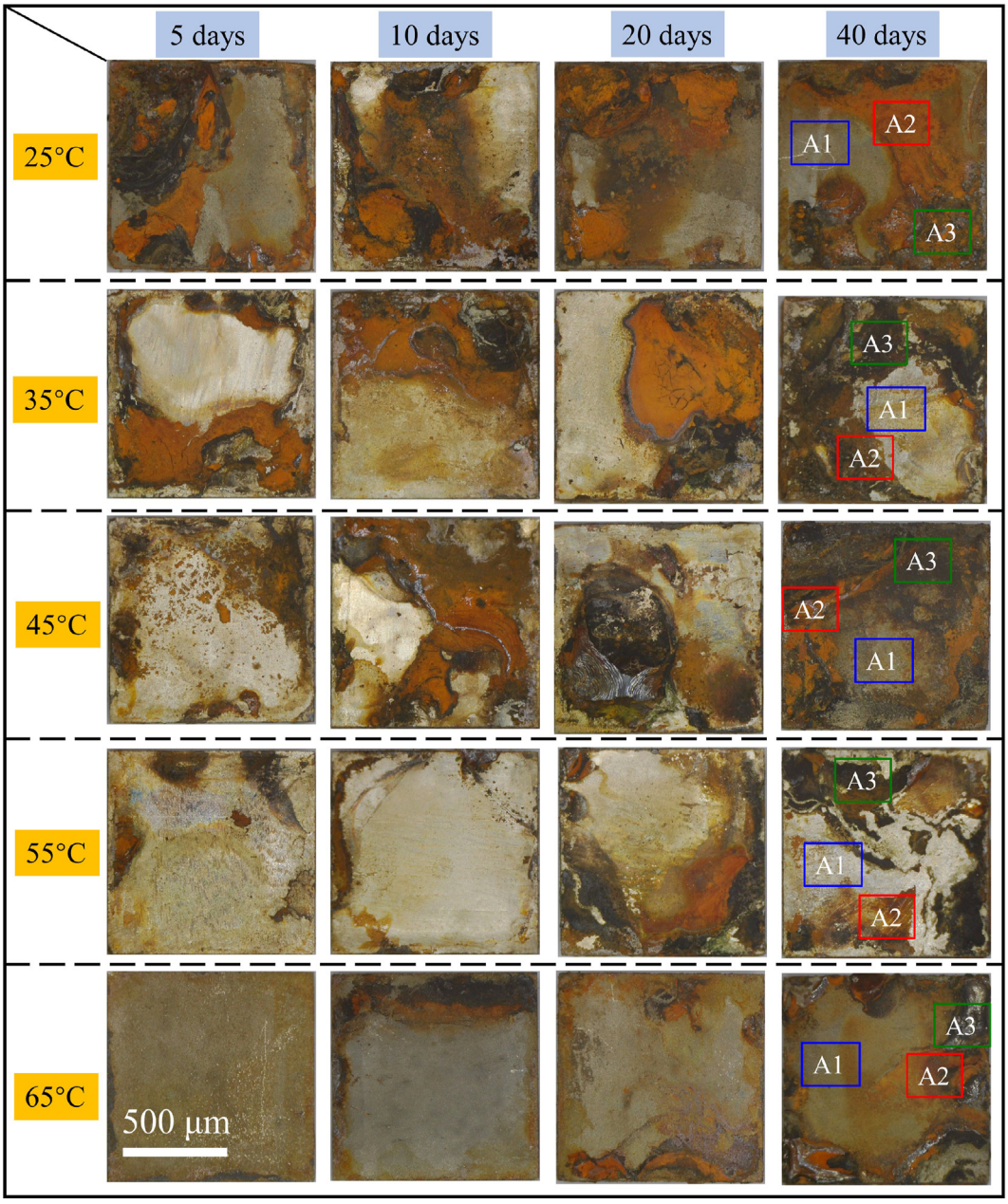

Fig. 11 – The optical images of the corroded Ni-Fe-WC coatings after NSS.

accurately calculate the internal stress of the coating. For the same diffraction surface (111), by changing different incident angles, measuring the corresponding diffraction angle 2θ, and obtaining the slope of 2θ versus sin2ψ, the internal stress can be calculated. As shown in the formula (4), σ_ψ is the internal stress, θ_0 is the Bragg Angle of the diffraction peak of the stress-free sample (PDF#37–0474), E is the elastic modulus (217 GPa), υ is poisson's ratio (0.33), ψ is the Angle of incidence (0°, 10°, 20°, 30°). The internal stress of Ni-Fe-WC composite coating prepared at different deposition temperatures is shown in Fig. 16. With the increase of deposition temperature from 25 °C to 65 °C, the internal stress of the coating is 194.7, 219.5, 232.2, 165.3 and 174.5 MPa, respectively.

$$\sigma_\psi = -\frac{E}{2(1+\upsilon)}\cot\theta_0\frac{\pi}{180}\frac{\partial(2\theta)}{\partial(\sin^2\psi)} \quad (4)$$

Researchers generally believe that the particles in the composite coating have an important effect on the residual stress. Ari-Gur et al. [42] electrodeposited Ni–SiC nano-composite coating on 2024-T3 aluminum substrate and found that the SiC particles have a greater impact on the crystal texture, residual stress, and mechanical properties of the

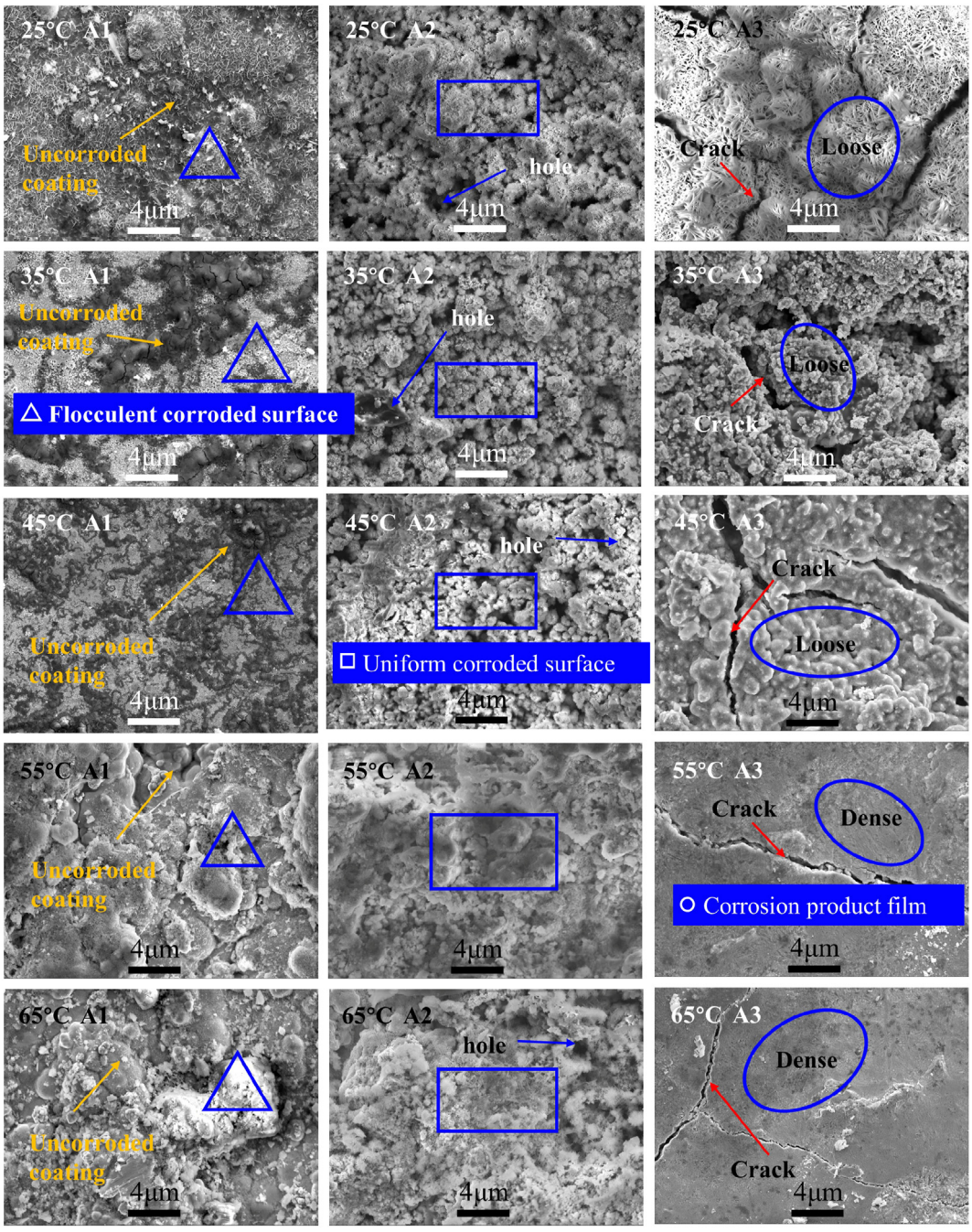

Fig. 12 – The surface morphologies of Ni-Fe-WC coatings after 40 days of NSS.

coating. Nanoparticles with smaller sizes produce compressive stress at lower concentrations and tensile stress at higher concentrations. Zhang et al. [43] studied the effect of ZrC particles on residual stress of Ni/ZrC composite coatings. With the increase of ZrC particles content in the coating, the texture of the coating decreases, and the internal stress decreases from 329.48 to 56.71 MPa. Górala et al. [44] analyzed the influence of alumina nanoparticles on the residual stress in the electrodeposited Ni/Al_2O_3 composite coating and found that the addition of alumina nanoparticles has a positive effect on the residual stress. When the concentration increases from 0 to 80 g/L, the residual stress of the coating decreases from 294 to 221 MPa. In the process of preparing Ni-Fe-WC composite coating by JED, when the temperature is low, as the deposition temperature increases, the deposition rate of the coating gradually increases, and the residual stress of the

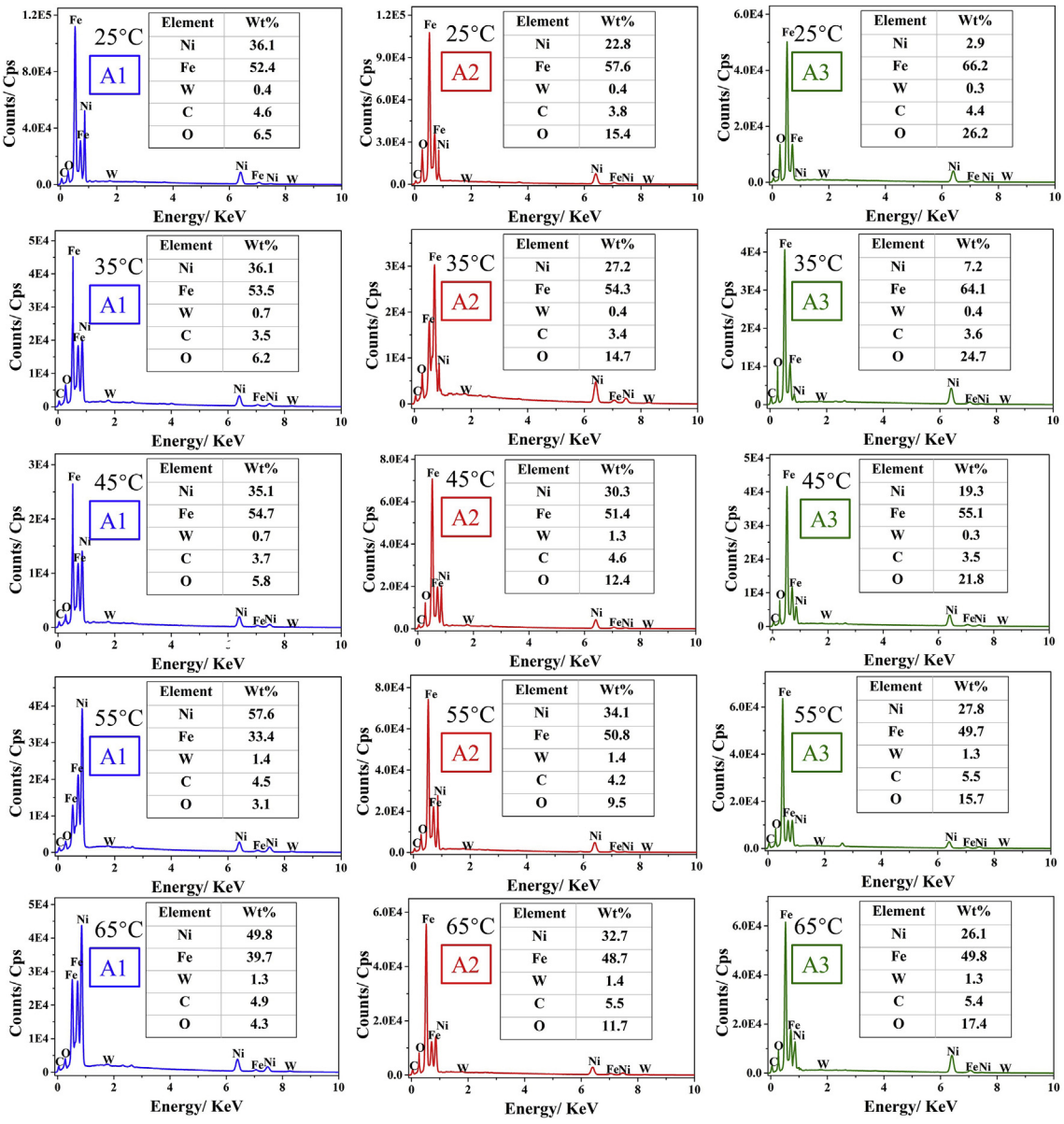

Fig. 13 – The EDS spectrums of Ni-Fe-WC coatings after 40 days of NSS.

coating gradually increases. However, when the deposition temperature increases to 55 °C, the WC particles content of coating increases significantly, while the residual stress of coating decreases obviously. This shows that WC particles are beneficial to reduce the residual stress of coating.

4.3. *Influence of WC particles on the coating corrosion resistance*

As shown in Fig. 17, the influence of temperature on the adsorption of WC particles in JED can be obtained. A large number of metal ions wrap single uniformly dispersed WC particle, which can be simplified into individual ion clusters [31]. The ion clusters quickly contact the substrate under the action of high-speed flushing solution (Fig. 17(a)). During the JED process, the particles near the substrate have the following states: The first state is that most of the particles rebound after contact and are washed away by the plating solution, and a small part of the WC particles are adsorbed on the substrate. According to the degree of adsorption, it is

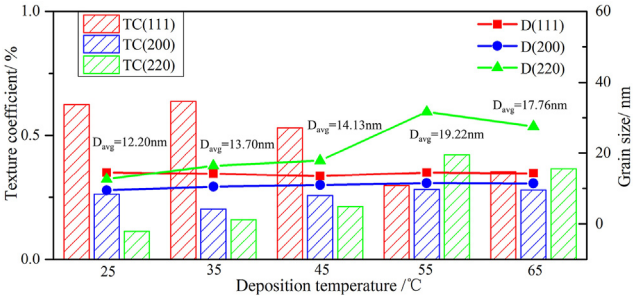

Fig. 14 – The average grain sizes and grain orientations of coatings.

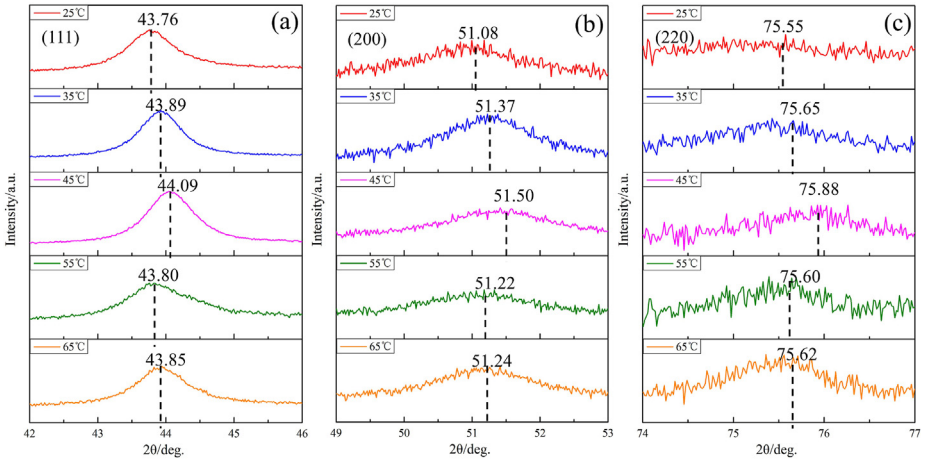

Fig. 15 – (a) (111), (b) (200) and (c) (220) plane peaks of coatings.

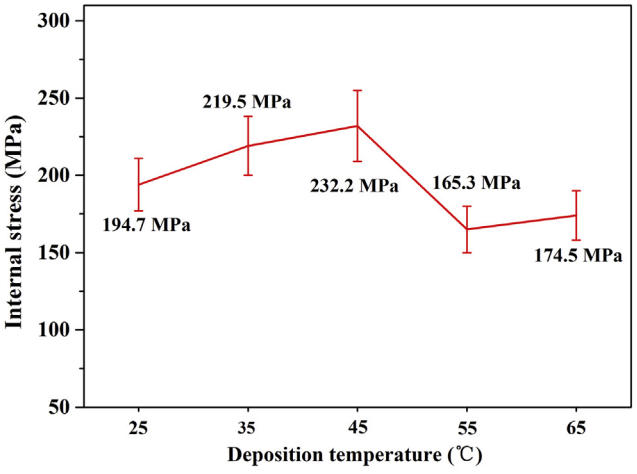

Fig. 16 – Internal stress of Ni-Fe-WC coatings.

divided into strongly adsorbed, intermediately adsorbed, and weakly adsorbed (Fig. 17(b)). According to the initial nucleation growth theory of composite co-deposition [45–48], the strongly adsorbed particles are irreversible, which means they must be surrounded by metal atoms to form a coating. The intermediately and weakly adsorbed particles stay on the surface of the substrate for a short period. During this period, if the reduced metal atoms cannot fully capture the particles, the particles will be washed away by the high-speed flowing plating solution. As shown in Fig. 17(c), when the temperature is low, the strongly adsorbed WC particles are all surrounded and fixed by the reduced Fe and Ni atoms. However, due to the low deposition temperature, the deposition rate of metal ions is relatively slow, the number of metal atoms reduced per unit time is small, the intermediately adsorbed WC particles cannot be fully captured, and the weakly adsorbed WC particles are not captured. As shown in Fig. 17(d), when the temperature is high, the deposition rate of metal ions is significantly higher than that at low temperatures. Except all strongly adsorbed WC particles are surrounded and fixed by reduced Fe and Ni atoms, most of the intermediately adsorbed WC particles and a small part of the weakly adsorbed WC particles are likely to be captured to form a composite coating. Therefore, as the deposition temperature increases, the content of WC particles in the composite coating increases. The nucleation growth mechanism of the Ni-Fe-WC coating preparation process is shown in Fig. 17(e-f). During the JED, the adsorbed WC particles affect the surrounding electric field distribution, and there will generally be fewer nucleation points and larger growth space around them. Since the size of WC particles is much larger than the size of surrounding grains, sufficient space is provided for nearby grains to grow, which can effectively release the internal stress of the coating.

The corrosion type of Ni-Fe-WC coating in this research mainly includes intergranular corrosion and stress corrosion cracking. Intergranular corrosion is a common type of coating corrosion, which generally extends to the inside along the interface between metal grains, and greatly reduces the performance of the coating by destroying the bond between the grains and even making it invalid [49,50]. Therefore, the larger the average grain size is, the smaller the proportion of grain boundary is, and the lighter the intergranular corrosion is. Stress corrosion cracking is caused by the release of stress in the coating during the corrosion process, which is likely to cause more serious damage to the coating. During the JED, a reasonable increase of deposition temperature is helpful to increase the WC particles content of Ni-Fe-WC coating. WC particles can promote grain growth and release internal stress in the coating, and significantly improve intergranular corrosion and stress corrosion.

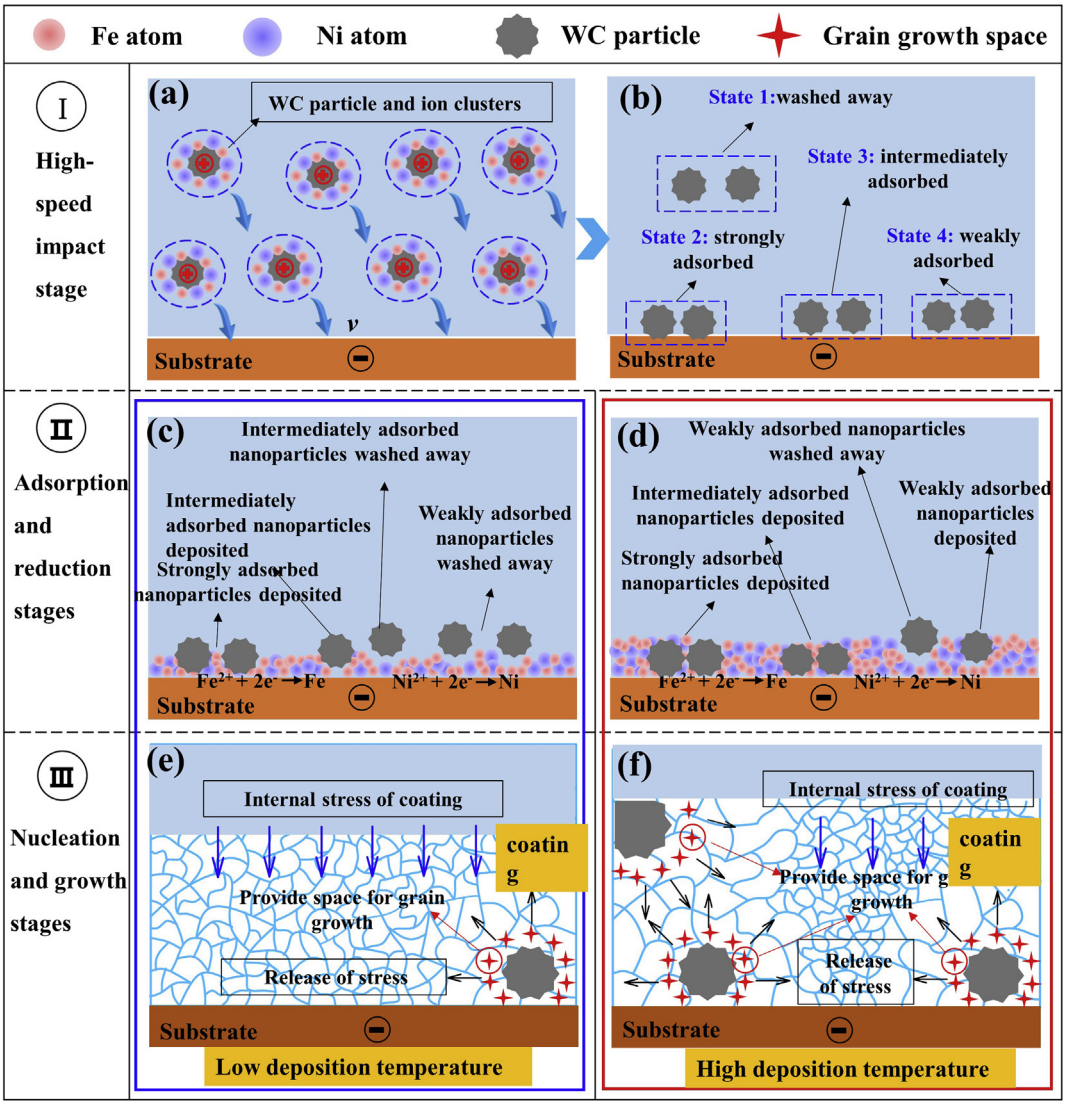

Fig. 17 – The schematic diagram of (a–d) WC particles adsorption mechanism and (e–f) nucleation growth mechanism of coating preparation process.

5. Conclusions

(1) The WC particles content of coating increased with the reasonable increase of temperature during the preparation of Ni-Fe-WC coating by JED. When the temperature is 55 °C, the highest WC particles content reaches 4.47 wt%.
(2) In the JED process, the grains around the WC particles have more space to grow, which can increase the average grain size and reduce internal stress.
(3) The more the WC particles in the Ni-Fe-WC coating, the stronger coating's ability to resist intergranular corrosion and stress corrosion.

Funding

This work was supported by the National Natural Science Foundation of China (Grant No. 51875579), the Independent Innovation Project of Central Universities (Grant No. 19CX02023A), the Source Innovation Project of Qingdao West Coast (Grant No. 2020–82), and the Science and Technology Support Plan for Youth Innovation of Universities in Shandong Province (Grant No.2019KJB016).

Declaration of Competing Interest

The authors declare that they have no known competing financial interests or personal relationships that could have appeared to influence the work reported in this paper.

REFERENCES

[1] Torabinejad V, Aliofkhazraei M, Sabour Rouhaghdam A, Allahyarzadeh MH. Corrosion properties of Ni-Fe-Cr (III) multilayer coating synthesized via pulse duty cycle variation. Mater Corros 2017;68:347–54.

[2] Torabinejad V, Aliofkhazraei M, Assareh S, Allahyarzadeh MH, Rouhaghdam AS. Electrodeposition of Ni-Fe alloys, composites, and nano coatings–A review. J Alloys Compd 2017;691:841–59.
[3] Torabinejad V, Aliofkhazraei M, Sabour Rouhaghdam A, Allahyarzadeh MH. Ni–Fe–Mn–(nano)Al_2O_3 coating with modulated composition and grain size. T Indian I Metals 2017;70:1199–207.
[4] Torabinejad V, Aliofkhazraei M, Sabour Rouhaghdam A, Allahyarzadeh MH. Functionally graded coating of Ni-Fe fabricated by pulse electrodeposition. J Mater Eng Perform 2016;25:5494–501.
[5] Chaudhari AK, Singh VB. A review of fundamental aspects, characterization and applications of electrodeposited nanocrystalline iron group metals, Ni-Fe alloy and oxide ceramics reinforced nanocomposite coatings. J Alloys Compd 2018;751:194–214.
[6] Xia M, Huang P, Cu R, Ge C. Cold sprayed W/Ni/Fe alloy coating: microstructure and mechanical properties. Surf Coating Technol 2016;291:376–81.
[7] Han B, Bei S, Han G, Du W, Zhu S, Yan X, et al. Surface characteristics of Ni-Fe-Cr-Nb-Al-Ti coatings by supersonic particle deposition and laser remelting on AlSi12Cu alloy. Opt Laser Technol 2020;132:106467.
[8] Guo J, Song C, Niu L, Shi X, Jin Z, Guo C, et al. Suppression of grain boundary steps in chemical mechanical polishing of W-Ni-Fe alloy by a citric acid-based slurry. Manu. Lett. 2020;25:40–3.
[9] Shankar G, Madhavan R, Kumar R, Sahoo B, Ray RK, Suwas S. Micro-mechanism of evolution of microstructure and texture in Ni-Fe alloys. Materialia 2020;13:100811.
[10] Yousefi E, Sharafi S, Irannejad A. The structural, magnetic, and tribological properties of nanocrystalline Fe-Ni permalloy and Fe-Ni-TiO_2 composite coatings produced by pulse electro co-deposition. J Alloys Compd 2018;753:308–19.
[11] Liu L, Peng J, Du X, Zheng H, Chen Z, Gong P, et al. Synthesis, composition, morphology, and wettability of electroless Ni-Fe-P coatings with varying microstructures. Thin Solid Films 2020;706:138080.
[12] Geng S, Qi S, Xiang D, Zhu S, Wang F. Oxidation and electrical behavior of ferritic stainless steel interconnect with Fe-Co-Ni coating by electroplating. J Power Sources 2012;215:274–8.
[13] Safavi MS, Babaei F, Ansarian A, Ahadzadeh I. Incorporation of Y_2O_3 nanoparticles and glycerol as an appropriate approach for corrosion resistance improvement of Ni-Fe alloy coatings. Ceram Int 2019;45:10951–60.
[14] Soares HJM, Campos OS, Dias DF, Casciano PNS, de Lima-Neto P, Correia AN. Chemical, morphological and corrosion characterisations of electrodeposited Ni-Fe-P coatings. Electrochim Acta 2018;284:18–23.
[15] Cui Z, Pei C, Wu S, Fu S, Guo C, Fang Y, et al. Ultrastable Ni-P amorphous alloy formed via high temperature electrodeposition. J Non-Cryst Solids 2021;551:120398.
[16] Rai PK, Gupta A. Investigation of surface characteristics and effect of electrodeposition parameters on nickel-based composite coating. Mater Today: Proceedings 2021;44:1079–85.
[17] Lee T, Chang L, Chen C. Effect of electrolyte temperature on composition and phase structure of nanocrystalline Fe–Ni alloys prepared by direct current electrodeposition. Surf Coating Technol 2012;207:523–8.
[18] Oliveira JAM, de Almeida AF, Campos ARN, Prasad S, Alves JJN, de Santana RAC. Effect of current density, temperature and bath pH on properties of Ni–W–Co alloys obtained by electrodeposition. J Alloys Compd 2021;853:157104.
[19] Seo MH, Dong JK, Kim JS. The effects of pH and temperature on Ni-Fe-P alloy electrodeposition from a sulfamate bath and the material properties of the deposits. Thin Solid Films 2005;489:122–9. 5.
[20] Starosta R, Zielinski A. Effect of chemical composition on corrosion and wear behavior of the composite Ni-Fe-Al_2O_3 coatings. J Mater Process Technol 2004;157–158:434–41.
[21] Li B, Mei T, Du S, Zhang W. Synthesis of Ni-Fe and Ni-Fe/ZrO_2 composite coating and evaluation of its structural and corrosion resistance. Mater Chem Phys 2020;243:122595.
[22] Rasooli A, Safavi MS, Babaei F, Ansarian A. Electrodeposited Ni-Fe-Cr2O3 nanocomposite coatings: a survey of influences of Cr_2O_3 nanoparticles loadings in the electrolyte. J Alloys Compd 2020;822:153725.
[23] Zhao Z, Liu D, Ma J, Chen X. Fluidization of nanoparticle agglomerates assisted by combining vibration and stirring methods. Chem Eng J 2020;388:124213.
[24] Xing S, Wang L, Jiang C, Liu H, Zhu W, Ji V. Influence of Y2O3 nanoparticles on microstructures and properties of electrodeposited Ni–W–Y2O3 nanocrystalline coatings. Vacuum 2020;181:109665.
[25] Li B, Li D, Mei T, Xia W, Zhang W. Fabrication and characterization of boron nitride reinforced Ni-W nanocomposite coating by electrodeposition. J Alloys Compd 2019;777:1234–44.
[26] Liu X, Shen L, Qiu M, Tian Z, Wang Y, Zhao K. Jet electrodeposition of nanocrystalline nickel assisted by controllable friction. Surf Coating Technol 2016;305:231–40.
[27] Ji L, Chen F, Huang H, Sun X, Yan Y, Tang X. Preparation of nickel–graphene composites by jet electrodeposition and the influence of graphene oxide concentration on the morphologies and properties. Surf Coating Technol 2018;351:212–9.
[28] Shen L, Xu M, Jiang W, Qiu M, Fan M, Ji G, et al. A novel superhydrophobic Ni/Nip coating fabricated by magnetic field induced selective scanning electrodeposition. Appl Surf Sci 2019;489:25–33.
[29] Xia FF, Jia WC, Ma CY, Yang R, Wang Y, Potts M. Synthesis and characterization of Ni-doped TiN thin films deposited by jet electrodeposition. Appl Surf Sci 2018;434:228–33.
[30] Wang C, Shen L, Qiu M, Tian Z, Jiang W. Characterizations of Ni-CeO_2 nanocomposite coating by interlaced jet electrodeposition. J Alloys Compd 2017;727:269–77.
[31] Jiang W, Shen L, Qiu M, Wang X, Fan M, Tian Z. Preparation of Ni-SiC composite coatings by magnetic field-enhanced jet electrodeposition. J Alloys Compd 2018;762:115–24.
[32] Ma C, Yu W, Jiang M, Cui W, Xia F. Jet pulse electrodeposition and characterization of Ni–AlN nanocoatings in presence of ultrasound. Ceram Int 2018;44:5163–70.
[33] Xu M, Shen L, Jiang W, Zhao F, Chen Y, Tian Z. Fabrication of Ni-SiC superhydrophilic surface by magnetic field-assisted scanning electrodeposition. J Alloys Compd 2019;799:224–30.
[34] Chen Q, Li J, Liao C, Hu G, Fu Y, Asare OK, et al. Ni foam supported NiO nanosheets as high-performance free-standing electrodes for hybrid supercapacitors and Ni–Zn batteries. J Mater Chem A 2018;6:19488–94.
[35] Suryawanshi MP, Ghorpade UV, Shin SW, Suryawanshi UP, Shim HJ, Kang SH, et al. Facile, room temperature, electroless deposited (Fe_{1-x},Mnx)OOH nanosheets as advanced catalysts:the role of Mn incorporation. Small 2018;14:1801226.
[36] Lv Y, Ding Y, Cui H, Liu G, Wang B, Cao L, et al. Investigation of microscopic residual stress and its effects on stress

corrosion behavior of NiAl bronze alloy using in situ neutron diffraction/EBSD/tensile corrosion experiment. Mater Char 2020;164:110351.
[37] Zhang F, Ji R, Liu Y, Li Z, Liu Z, Lu S, et al. Defect-rich engineering and F dopant Co-modulated NiO hollow dendritic skeleton as A self-supported electrode for high-current density hydrogen evolution reaction. Chem Eng J 2020;401:126037.
[38] Zhang F, Ji R, Liu Y, Pan Y, Cai B, Li Z, et al. A novel nickel-based honeycomb electrode with microtapered holes and abundant multivacancies for highly efficient overall water splitting. Appl Catal B-Environ 2020;276:119141.
[39] Ji R, Han K, Jin H, Li X, Liu Y, Liu S, et al. Preparation of Ni-SiC nano-composite coating by rotating magnetic field-assisted electrodeposition. J Manuf Process 2020;57:787–97.
[40] Lumbeeck G, Delvaux A, Idrissi H, Proost J, Schryvers D. Analysis of internal stress build-up during deposition of nanocrystalline Ni thin films using transmission electron microscopy. Thin Solid Films 2020;707:138076.
[41] Delvaux A, Lumbeeck G, Idrissi H, Proost J. Effect of microstructure and internal stress on hydrogen absorption into Ni thin film electrodes during alkaline water electrolysis. Electrochim Acta 2020;340:135970.
[42] Ari-Gur P, Sariel J, Vemuganti S. Residual stresses and texture in Ni/SiC nanocomposite coatings. J Alloys Compd 2007;434–435:704–6.
[43] Zhang Z, Jiang C, Liao Z, Wei G. Effect of electrodeposition parameters on the evolution of crystallographic texture and internal stress of Ni/ZrC composite coatings. Mater. Today. Commun. 2021;27:102403.
[44] Góral A, Skrzypek SJ. The influence of alumina nanoparticles on lattice defects, crystallographic texture and residual stresses in electrodeposited Ni/Al_2O_3 composite coatings. Appl Surf Sci 2018;456:147–55.
[45] Fransaer J, Celis JP, Roos JR. Analysis of the electrolytic codeposition of non-brownian particles with metals. J Electrochem Soc 1992;139:413–25.
[46] Tan CY, Liu Y, Zhao XS, Zheng ZQ. Nickel co-deposition with SiC particles at initial stage. T. Nonferr. Metal. Soc. 2008;18(5):1128–33.
[47] Guglielmi N. Kinetics of the deposition of inert particles from electrolytic baths. J Electrochem Soc 1972;119:1009.
[48] Celis JP, Roos JR, Buelens C. A mathematical model for the electrolytic codeposition of particles with a metallic matrix. J Electrochem Soc 1987;134:1402–8.
[49] Zhang J, Xu L, Han Y, Zhao L, Xiao B. New perspectives on the grain boundary misorientation angle dependent intergranular corrosion of polycrystalline nickel-based 625 alloy. Corrosion Sci 2020;172:108718.
[50] Zhang X, Lv Y, Shan F, Wu Y, Lu X, Peng Z, et al. Microstructure, corrosion resistance, osteogenic activity and antibacterial capability of Mn-incorporated TiO_2 coating. Appl Surf Sci 2020;531:147399.